Analysis of Solar Hemispheric Chromosphere Properties using the Kodaikanal Observatory Ca–K Index

Partha Chowdhury[1] , Ravindra Belur[2] , Luca Bertello[3] , and Alexei A. Pevtsov[3]

[1] University College of Science and Technology, Department of Chemical Technology, University of Calcutta, 92, A.P.C. Road, Kolkata, 700009, West Bengal, India; parthares@gmail.com, partha240@yahoo.co.in
[2] Indian Institute of Astrophysics, Koramangala, Bengaluru-560034. India
[3] National Solar Observatory, 3665 Discovery Drive, Third Floor, Boulder, CO 80303, USA

Abstract

The Kodaikanal Observatory has provided long-term synoptic observations of chromospheric activities in the Ca II K line (393.34 nm) since 1907. This article investigates temporal and periodic variations of the hemispheric Ca–K-index time series in the low-latitude zone ($\pm 40°$), utilizing the recently digitized photographic plates of Ca–K images from the Kodaikanal Observatory for the period of 1907–1980. We find that the temporal evolution of the Ca–K index differs from one hemisphere to another, with the solar cycle peaking at different times in the opposite hemisphere, except for cycles 14, 15, and 21, when the phase difference between the two hemispheres was not significant. The monthly averaged data show a higher activity in the northern hemisphere during solar cycles 15, 16, 18, 19, and 20, and in the southern hemisphere during cycles 14, 17, and 21. We notice an exponentially decaying distribution for each hemisphere's Ca–K index and the whole solar disk. We explored different midterm periodicities of the measured Ca–K index using the wavelet technique, including Rieger-type and quasi-biennial oscillations on different timescales present in the time series. We find a clear manifestation of the Waldmeier effect (stronger cycles rise faster than the weaker ones) in both the hemispheres separately and the whole disk in the data. Finally, we have found the presence of the Gnevyshev gap (time interval between two cycle maxmima) in both the hemispheric data during cycles 15 to 20. Possible interpretations of our findings are discussed with the help of existing theoretical models and observations.

Unified Astronomy Thesaurus concepts: Solar cycle (1487); Active sun (18); Solar chromosphere (1479); Plages (1240)

1. Introduction

The Sun is a dynamic star whose different activities vary on a timescale from seconds to centuries. Apart from the well-known cyclic trend of ~11 yr (sunspot cycle), solar indices often exhibit different short-term and midterm periodicities, such as Rieger-type periodicities (130–190 days) and the quasi-biennial oscillations (QBOs) in the range of 1.2 to 3.5 yr (e.g., Bazilevskaya et al. 2014, for details). Moreover, the long-term behavior of different solar activity indices in the northern and southern hemispheres show an asymmetric nature with a temporal phase shift (Waldmeier 1957; Carbonell et al. 1993; Hathaway 2015, and references therein). This phenomenon is known as "North–South" (N–S) asymmetry, which indicates that the strength of the cycle is different in northern and southern hemispheres. The N–S asymmetry in solar activity indices and their solar cycle variations have some important implications for the solar magnetic field generation and its periodicity (e.g., Norton et al. 2014, for detailed review).

Originally, N–S asymmetry has been detected in the distribution of solar flares and sunspots. This hemispheric imbalance was also detected during the Maunder minimum (1645–1715), when the solar activities were exteremely low, and it was strongly south-dominated (Sokoloff & Nesme-Ribes 1994). However, observations in Ca K line may offer additional clues as they show the solar magnetic features, which may not have a white light features such as pores and sunspots. The Ca II K line, centered at 393.367 nm, is a handy diagnostic tool to study long-term solar chromospheric activities (Schrijver et al. 1989; Donahue & Keil 1995; Foukal et al. 2006; Livingston et al. 2007; Ermolli et al. 2014; Bertello et al. 2020). The intensity of the Ca–K emission line can be used as a proxy to measure the chromospheric emission (Foukal et al. 2009) as well as the total solar magnetic flux (Ermolli et al. 2009, 2010; Chatzistergos et al. 2019). It has been reported that Ca–K plages and networks account for about one-half of the total magnetic flux of the Sun and are responsible for most of the variations in ultraviolet flux and total solar irradiance (TSI) (Foukal 1996; Krivova et al. 2003; Fontenla et al. 2015; Chatzistergos et al. 2018). The solar cycle variations in the Ca–K time series play a significant role in understanding the behavior of the solar dynamo because the intensity of the Ca–K line is a good proxy for Sun's magnetic flux density (Pevtsov et al. 2016; Chatzistergos et al. 2019, etc.).

The Ca–K plages are produced from complex magnetic processes and are the extension of the photospheric faculae up to the chromosphere. Plages are mainly located above those regions where sunspot groups formed. These features can change their shape and size during their lifetime. However, plages remain to exist even after the decay of their associated sunspots. Plages may also be associated with small active region-like magnetic field structures, in which sunspots may never form. Several investigations of different dynamical properties of the plages, including their periodic behavior using the historical full-disk observations have been conducted

in recent years (e.g., Chowdhury et al. 2016; Pevtsov et al. 2016; Bertello et al. 2020; de Paula & Curto 2020). These studies may provide valuable information about long-term solar variation and its impact on the Earth's climate (Chatzistergos et al. 2018, 2019).

Kodaikanal Observatory in India provides a long-term, homogeneous time series of Ca–K plages through spectroheliograms of the Sun since 1907 (Hasan et al. 2010; Bertello et al. 2016). This paper analyzes multiple decades of Ca–K observations at Kodaikanal Observatory to investigate several distinctive properties of this data set, like hemispheric asymmetry, phase asynchrony, Waldmeier effect, and Gnevyshev gap. We also study quasi-periodic oscillations present in the Ca–K time series separately for each hemisphere.

In Section 2, we briefly describe the data. In Section 3, we present the results of our investigation, and in Section 4, we draw a brief discussion and conclusion.

2. Data

In the present investigation, we have utilized the monthly average value of Ca–K plage index (Ca–K index or plage index) time series for both the hemispheres, measured at Kodaikanal Observatory (KO), India. The KO has archived full-disk Ca–K observations. These images are captured in photographic plates, observed through an unaltered telescope having a 30 cm objective lens, with f/21 (Priyal et al. 2014). These photographic plates were digitized using a 16-bit digitizer. The calibration process, including data reduction, quality of the images, and digitization of the Ca–K spectroheliograms, were described by Priyal et al. (2014, 2017); Chatterjee et al. (2016). From these digitized and calibrated images, Chatterjee et al. (2016) identified the plage regions. Following Bertello et al. (2010); Chatterjee et al. (2016) have computed the Ca–K index using the digitized Ca–K images. The new digitized and calibrated versions of these data are available for scientific use at https://kso.iiap.res.in.

Photospheric features such as sunspots are mainly concentrated within the toroidal belts, i.e., within ±40° of the equator (Hathaway 2015). The strongest plages are also restricted within the same latitude range as above (Solanki & Krivova 2009). A similar distribution of plages was detected in the "butterfly diagram" prepared by Chatterjee et al. (2016) using Ca–K images of KO. Therefore, we have restricted our Ca–K index analysis within –40° to +40° of the latitude belt in both the hemispheres. The variations of this index within this latitude belt indicate the change in the large-scale magnetic field on the Sun. The complete time series of the Ca–K plages measured at KO spans more than 100 yr (1907–2007). However, it appears that the "Good" data set is available until 1980 (for definition, see Priyal et al. 2019), and later data either have significant time gaps or poor contrast (Priyal et al. 2019). Hence, we have restricted our analysis to the period between 1907 and 1980, covering the declining phase of cycle 14 to cycle 21 (only rising branch that includes maximum). We have made overplot of the recently digitized Ca–K plage time series measured at the Mount Wilson Observatory (MWO) (Bertello et al. 2010, 2020) for the time interval 1915–1980 to compare the nature and variation with KO time series. Further, to compare with Ca–K index and sunspot activities, we used the Greenwich monthly sunspot area time series of the opposite hemispheres, for the same time period, available from the website http://solarcyclescience.com/activeregions.html.

The plage index data is obtained from Chatterjee et al. (2016). They have detected the plages in the calibrated images (Priyal et al. 2014) by applying the histogram equalization method and global thresholds. By following this technique and using the method explained in Bertello et al. (2010), they have computed the plage index. The plage index was computed latitude-wise and using the same data we have used in this study. Here, we compute the plage index separately for the northern and the southern hemisphere. A typical digitized and calibrated calcium image obtained on 1918 February 12 at KO is shown in Figure 1(top left and right). Carrington rotation (CR) maps are very useful for studying the solar activities' dynamical behavior and their variation at every location on the solar surface. Sheeley et al. (2011); Bertello et al. (2020) have generated and studied the complex behavior of the Ca–K plages in different solar cycles from Mt. Wilson images. Here, we present one CR map generated from the Ca–K images from the KO database to describe some features of the plages (Figure 1 bottom). Carrington maps show the full 360° view of the Sun. In the map, large-scale magnetic fields can be identified easily. These maps are useful to identify the active longitude and latitude as the cycle progress. The one shown in Figure 1(bottom) is constructed for the Carrington rotation number 741, which spans from 1909 February 13 to March 13. In the map, the white patches are the plage regions. Detailed descriptions of the individual CR maps are given on the website of the KO and in the paper of Chatterjee et al. (2016).

3. Results

3.1. Solar Cycle Variation and Size Distribution of Ca–K Index

Figure 2 shows the yearly averaged Ca–K plage index of both the hemispheres and the full solar disk measured at the KO (blue color) overplotted with the MWO data (red color). This Figure indicates that the Ca–K index in both hemispheres follows a regular cyclic pattern of about 11 yr, and the dynamical behavior is different in each solar cycle under study. This Figure shows that the even-numbered solar cycles (cycles 16 and 20) have lower peak values compared to the preceding odd-numbered solar cycles (cycles 15 and 19) in north, south, and the sum of these two data sets. This behavior follows the odd–even cycle rule (Gnevyshev & Ohl 1948). However, we have found that peak height during cycle 18 is higher than preceding odd-cycle 17 in all the data sets. So, in the case of cycles 17 and 18, this odd–even cycle rule was not maintained. Using sunspot number, Zolotova & Ponyavin (2015) showed that cycles 17–18 do not follow the odd–even rule. But they do follow the even–odd rule (see also: Hathaway 2015). The maximum amplitude of the plage index occurred during solar cycle 19, and cycle 18 is the second one for the northern hemisphere and full-disk. However, in the southern hemisphere, the amplitude of cycles 18 and 19 are nearly equal. Apart from this, the ascending branch of cycle 21 shows relatively high values and comparable with cycle 19 in the southern hemisphere and full solar disk data. Within the period of our analysis, cycle 16 exhibits the weakest peak value in both the opposite hemispheres and the whole disk. This result is in agreement with the behavior of international sunspot number. This result supports a conclusion that cycle 16 had lowest level of activity both in strong active regions, which hosted sunspots and pores, and weaker plage fields, which may not have sunspots associated with them.
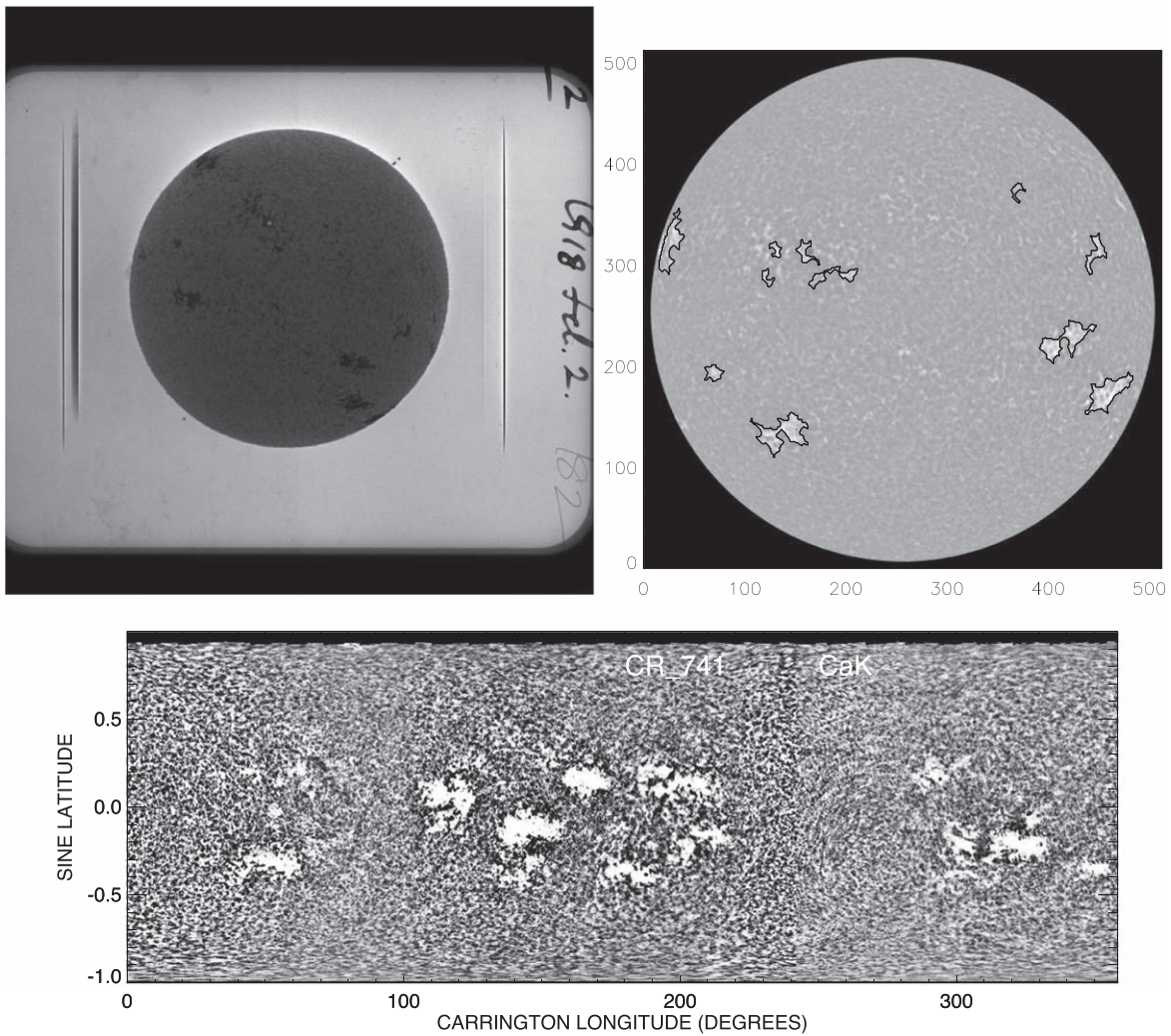
Figure 1. Top left: a sample digitized image of the Sun taken in Ca–K 3933 Å wavelength recorded on the photographic plate. The image is taken on 1918 February 12. Top right: the calibrated image with reduced in size. The detected plages are shown with the contours overlaid on it. Bottom: the sample Carrington map in Ca–K for the rotation number 741 spanning a period from 1909 February 13 to 1909 March 13. The abscissa is a longitude measured in degrees, and the ordinate is the sine of latitude.

Further, we notice double peaks in the Ca–K index time series during solar cycles 16, 18, 19, and 20 for the northern hemisphere. The double peak in cycles 15 and 17 is less prominent. Whole disk data exhibits very prominent double peaks during cycles 16 and 18, whereas both the hemispheres show spike-like peaks during their decay phase in cycle 20. In cycle 19, no such double peak is observed in the whole-disk data, but both hemispheres have unique double-peak signatures. The presence of double peaks in plage distribution in each hemisphere suggests that the origin of double peaks in sunspot numbers is not simply due to a temporal shift of activity peaks in northern and southern hemispheres, but due to the subphotospheric dynamo itself.

As we are interested to study about the association of the Ca plage data between KO and MWO, we plot the values of the yearly averaged data. From Figure 2, we readily see that these two time series exhibit a good match with each other. Most of the features, including the double peaks seen in the KO plage time series, are also present in the MWO plage data. In the case of the northern hemisphere, the correlation coefficient is ∼0.81, and for the southern hemisphere, it is ∼0.87 between these two observatories. For the whole-disk data, the correlation

coefficient is ∼0.96 between KO and MWO data sets. However, there exists some differences between these two data sets that are mainly found in the hemispheric time series. For cycles 16, 17, and 18, the double-peak nature of KO plage data in the northern hemisphere is slightly different than MWO data. The southern hemisphere is prominent in case of cycle 17. Cycle 20 shows some complex structure in both the hemispheres for both the stations' data sets. The whole-disk KO data exhibits distinct dual peaks during the maxima of the cycle 18, which is absent in MWO data. The peak of MWO plage data during cycle 20 is flat in comparison with KO data. However, we notice a good overall match between the two data sets with a very high correlation except for the rising branch of cycle 21 in the case of the southern hemisphere and the full disk. This difference during cycle 21, may be due to the availability of small number good images per year between 1978 and 1980 in KO (Priyal et al. 2019). Previously Chatterjee et al. (2016) also detected a strong correlation with KO plage index and MWO fractional plage area.

The Ca–K plages possess a variety of sizes, and it also varies in the course of different phases of the solar cycle. Figure 3 presents the histogram plot of the size variations of plages for
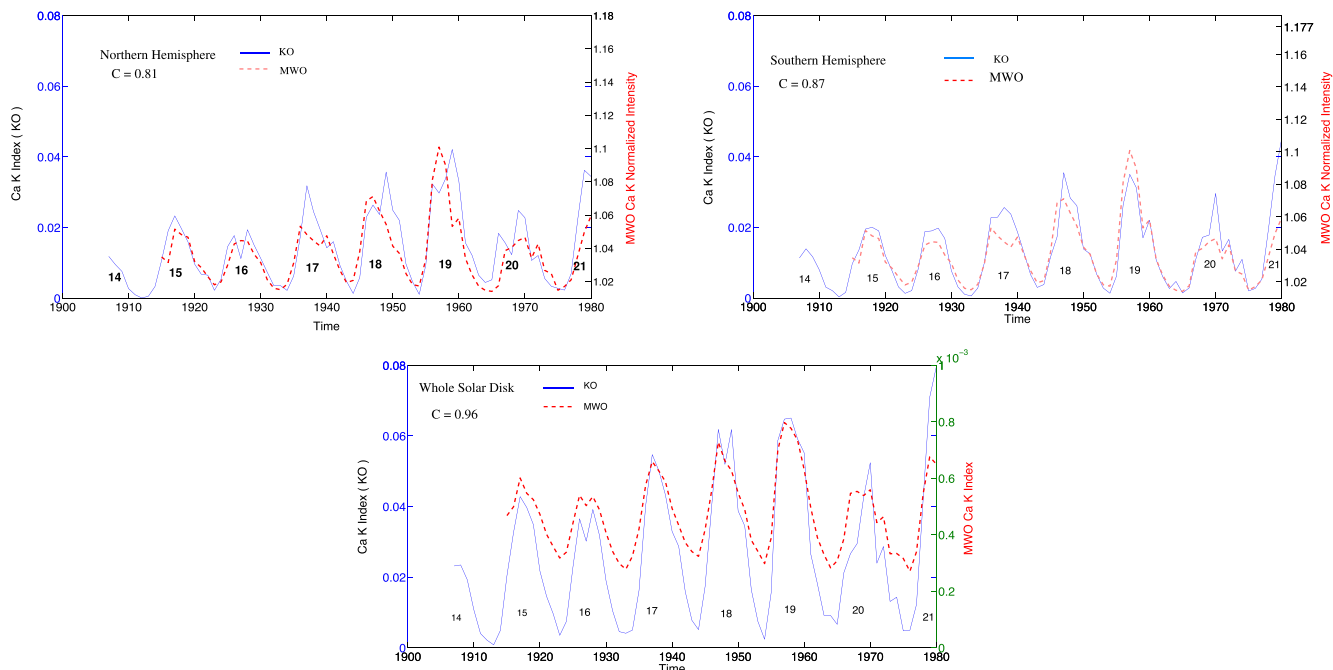
Figure 2. Temporal variations of the yearly averaged Ca–K Index measured at KO overplotted with MWO plage data for cycles 14–21. Top left: northern hemisphere. Top right: southern hemisphere. Bottom: whole solar disk. Solar cycle numbers are also labeled on the figures.
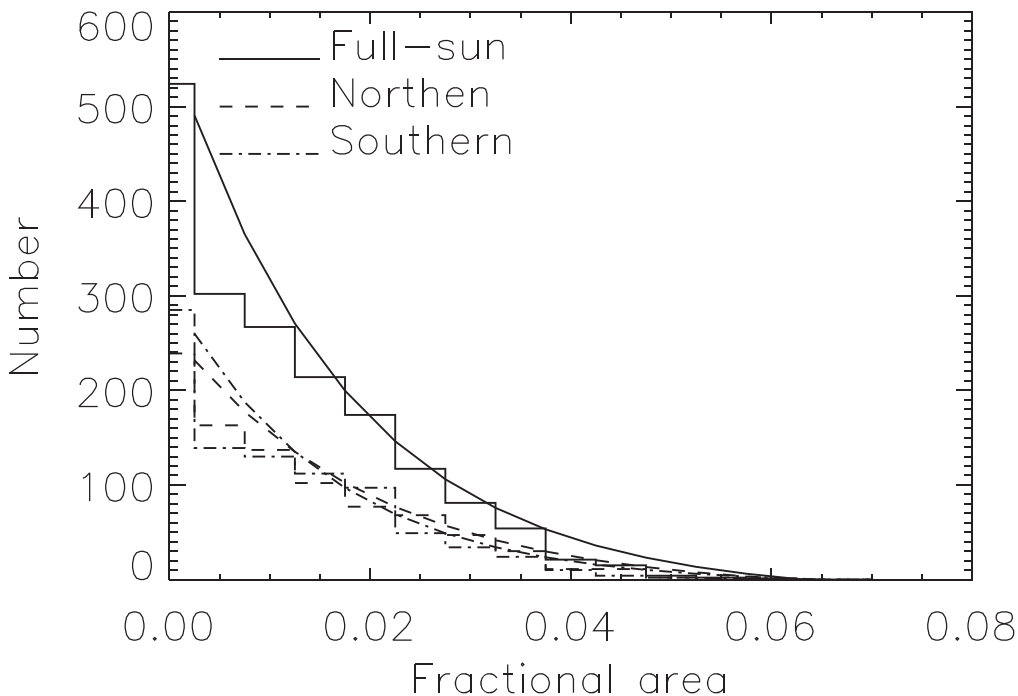
Figure 3. Histograms of fractional area is shown for the northern, southern and full-disk Ca–K index data. The dash, dashed–dotted and thick curves are exponential fit to the N, S, and full-disk histograms, respectively. The functional form of the exponential fit is $y = 276.3e^{(-x/0.02)} - 11.7$ for the north, $y = 310.4e^{(-x/0.016)} - 4.87$ for the south, and $y = 584.1e^{(-x/0.018)} - 15.96$ for the full-disk histogram plot.

both hemispheres and the full disk. We have tested different models to fit the histogram data, and computed their corresponding reduced chi-square statistic. We found that an exponential function produces the best match between observations and estimates. Hence, we fit all the histograms with a decaying exponential function which is shown by black, blue, and red-colored solid lines for the N, S, and whole-disk fractional area data, respectively. The decaying exponential function is given in the figure caption.

Sunspots and Ca–K plages appear in two different layers of the Sun. They almost emerge together or formed one after another when the sunspot is going to disperse its magnetic fields. To find the relationship between these two quantities, we made scatter plots (annual average) which are shown in Figure 4(top left, right and bottom). For the northern hemisphere, the correlation coefficient is ∼0.81, and for the southern hemisphere, it is ∼0.79 between these two structures. The correlation coefficient is ∼0.95 when the whole disk is
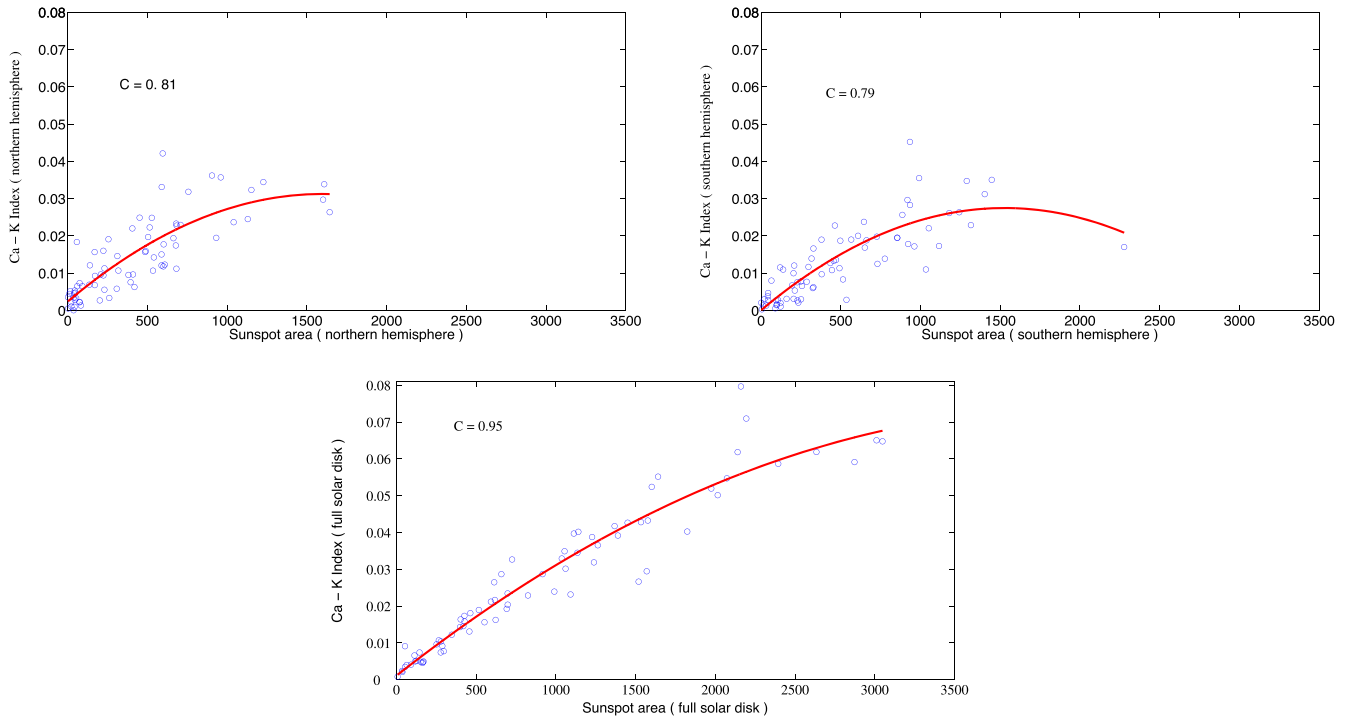
Figure 4. Scatter plot between the yearly averaged Ca–K index and the sunspot area. Top left is for the northern hemisphere, top right is for the southern hemisphere and the bottom plot is for the whole solar disk plage index data. The correlation coefficients are also shown in each plot.

considered. Observationally, not all plages may host sunspots, and there is often a lag between the development of plages and the appearance of sunspots inside the plages. Thus, these high correlation coefficients between sunspot and plage numbers are likely due to their mutual dependence on solar cycle variations. The high correlation coefficient confirms the close association of these two different solar features within the latitude band of $-40°$ to $+40°$. We have found that nonlinearity between these two data sets are weak, and we fit a second-order polynomial to the data points, and we found that $y = -1.131 \times 10^{-8} x^2 + 3.613 \times 10^{-5}(\pm 0.01)x + 2.4 \times 10^{-3}$ fits well for the northern hemisphere. A similar second-order polynomial for the x value is obtained for the southern hemisphere ($y = -1.176 \times 10^{-8} x^2 + 3.591 \times 10^{-5}(\pm 0.01)x + 6.34 \times 10^{-5}$) and whole-disk data ($y = -3.99 \times 10^{-9} x^2 + 3.40 \times 10^{-5}(\pm 0.02)x + 1.11 \times 10^{-3}$). This suggests that the relationship is not linear, at least for the larger sunspot and plage groups. This also suggests that the difference in distributions of plages by size is likely due to their dynamo origin, not due to the dissipation process after magnetic field emergence.

### 3.2. North–South Asymmetry of Ca–K Index

From Figure 2, we notice that the evolution of the Ca–K index with the solar cycle is not symmetric in its opposite hemispheres. Following Hathaway (2015), the hemispheric imbalance or the N–S asymmetry is defined as $A = (N_{ca} - S_{ca})/\sqrt{(N_{ca} + S_{ca})}$, where N_{ca} and S_{ca} are the monthly/yearly mean value of Ca–K index in the northern and southern hemispheres, respectively. We computed the values of the "asymmetry index" (A) for the Ca–K time series and their yearly variations are shown in Figure 5(left). The value of A may be considered as the measure of this difference.

From Figure 5(left), we notice that during the minima of cycles 15, 16, 17, 18, and 19, the northern hemisphere dominates, whereas for the minima of the rest cycles, like 14 and 20, the southern hemisphere dominates. The southern hemisphere was also more active during the onset and rising phases of cycles 17 and 18. Further, we see that the northern hemisphere dominates during the ascending phase of cycles 15, 16, 19, 20, and 21. The southern hemisphere exhibits excess activity around the maxima of cycles 16, 18, and 19. On the other hand, the northern hemisphere was more active around the maxima of 15, 17, and 20.

Further, to understand the trend of evolution of the "asymmetry index" in different solar cycles under study, we have drawn lines by looking at the trend in the scattered points of the monthly values of asymmetry index for each cycle (Figure 5 right). The plot shows that there is a slow change in the slope from Cycle 15 to 17. After that, the sign of the slope changes suddenly in cycle 18 and then reverses back in cycle 19. We have only six complete solar cyles of Ca–K data. Hence, to examine whether there is any periodicity in the asymmetry, we need to have a few more cycles of data.

3.3. Cumulative Counts and Dominant Hemispheres

The cumulative sum of the monthly average Ca–K index for solar cycles 14 (descending phase only) to 21 (ascending phase only) is shown in Figure 6. In the Figure, The Ca–K indices in the northern and southern hemispheres are indicated by solid and dashed lines, respectively. We notice that cycles 16 and 21 (only ascending branch) show approximately equal activity levels in both hemispheres. The northern hemisphere was more active during cycles 15, 18, 19, and 20. However, in solar cycles 14 (descending phase only) and 17, the southern hemisphere dominated the northern hemisphere. The cumulative plots indicate that during cycles 19 and 20, the northern
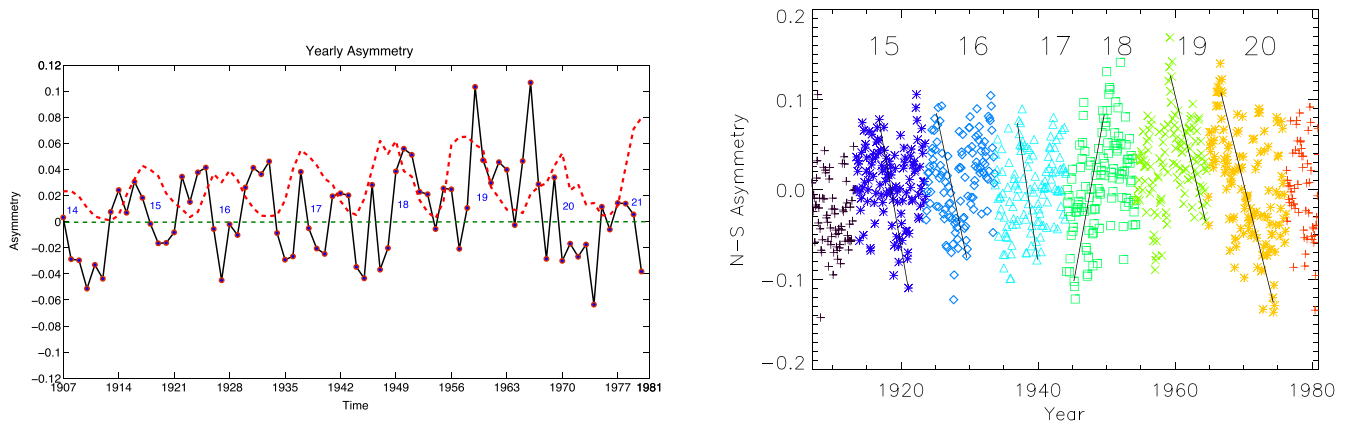
Figure 5. Left: Temporal evolution of the yearly averaged, asymmetry index of Ca–K index data points of Cycles 14–21. The yearly averaged Ca–K index is shown in red dashed lines. Right: The asymmetry index in the monthly mean Ca–K index is plotted against time. The solid lines in the right-side plot indicate the trends during each cycle under study.
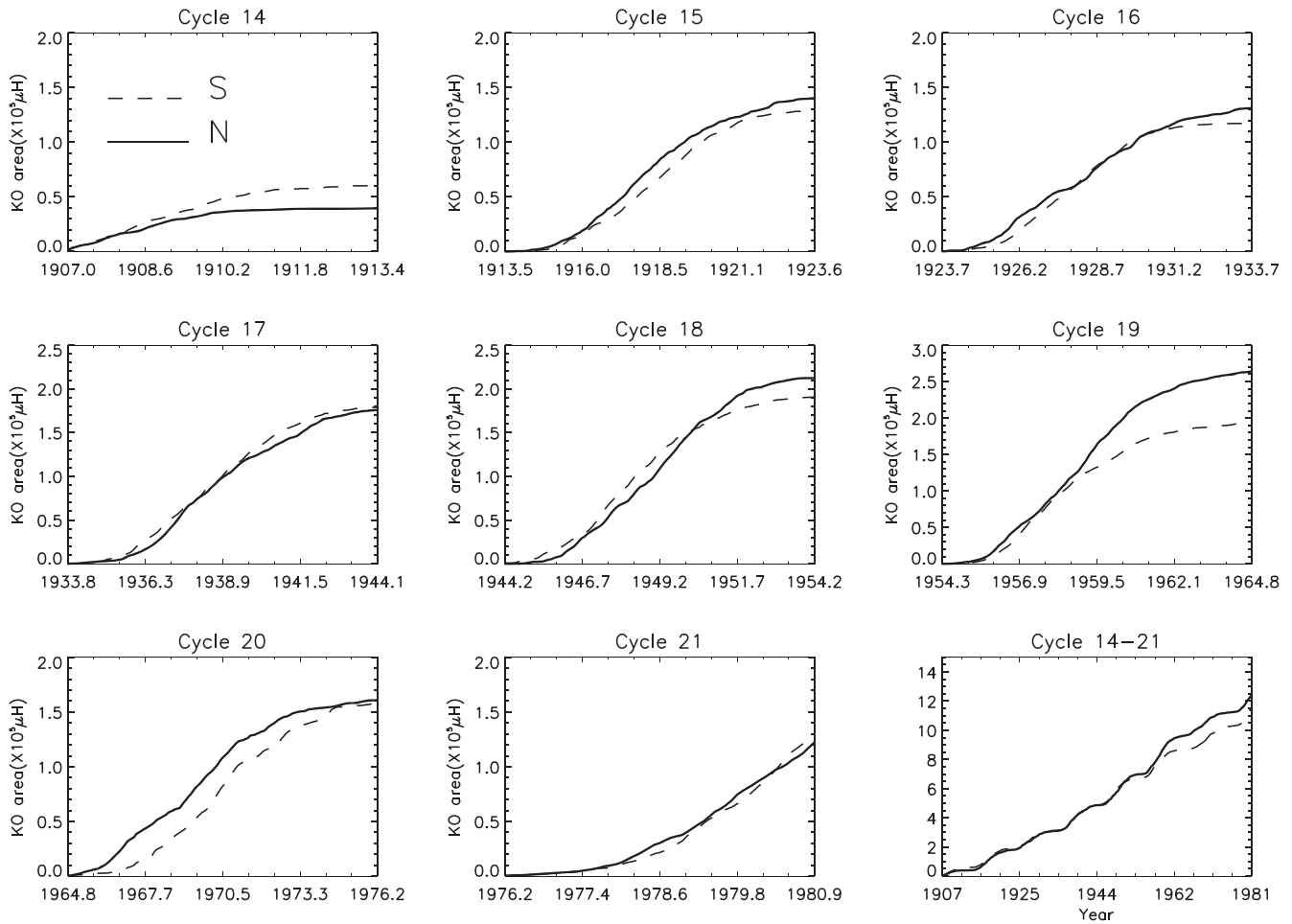
Figure 6. Cumulative monthly counts of Ca–K index for solar cycles 14–21. The bottom-right plot is for all the cycles, starting from 1907 to 1980.

hemisphere's activity was always dominant, a unique property of these two cycles. The bottom-right plot in Figure 6 exhibits the cumulative sum of the Ca–K index for the northern and southern hemispheres for cycles 14–21. This plot shows a small or vanishing asymmetry before cycle 19, and after that, there is a small dominance of the northern hemisphere. This is because,

during solar cycles 19 and 20, the activity was higher in the northern hemisphere compared to the southern.

To determine the dominant hemisphere in each solar cycle, we have computed a t-test (Carbonell et al. 2007), and the results are presented in Table 1. When the probability value of the t-distribution is <0.025 (statistical significance level

Table 1
Asymmetry and Dominant Hemispheres of Ca–K Index for Cycles 14–21

Cycle	Ca–K index in North hemi (monthly ave)	Ca–K index in South hemi (monthly ave)	Probability	Asymmetry	Dominant
14 (d-phase only)	0.39	0.6	5.49×10^{-6}	−0.211	S
15	1.4	1.29	4.64×10^{-2}	0.067	None
16	1.31	1.18	4.13×10^{-2}	0.082	None
17	1.76	1.79	3.65×10^{-1}	−0.015	None
18	2.12	1.91	2.69×10^{-2}	0.104	None
19	2.69	1.94	3.34×10^{-8}	0.322	N
20	1.62	1.59	4.01×10^{-1}	0.016	None
21 (r-phase only)	1.22	1.27	2.75×10^{-1}	−0.031	None

Note. In the Table d-phase means the descending phase and r-phase means rising phase. In the last column, "S" means the southern hemisphere and "N" means the northern hemisphere.

>95%), then the asymmetry value in the Ca–K index data during a particular solar cycle is statistically significant. Otherwise, the difference between the two hemispheres for any cycle should be regarded as marginal and written as "none" in the table.

Table 1 shows that the probability of the hemispheric asymmetry is statistically significant for the southern hemisphere in cycle 14 and the northern hemisphere during cycle 19. The southern hemisphere is preferred in solar cycles 17 and 21 (ascending phase), but the difference is not statistically significant. Similarly, the Ca–K index activity in the northern hemisphere was more in cycles 15, 16, 18, and 20. Therefore, it is evident that, on average, the northern hemisphere dominates over the southern one for the cycles analyzed here. Our analysis of the long term hemispheric asymmetry and the prefered hemispheres in Ca–K index during different parts of the different cycles under study are closely consistent with the asymmetric nature of sunspot area time series as shown by Zolotova et al. (2010).

3.4. Periodicities in the Ca–K index

Here we investigate the short-term and midterm periodic variations (⩾3 months and ⩽11 years) present in the monthly averaged Ca–K index data obtained from the KO. The variations of this index in a short timescale provide information about the dynamics and energy transport in the chromosphere, whereas the long-term variations indicate the dynamo operation.

We have considered the data of the northern, southern hemisphere, whole spheres, and the N–S asymmetry separately for this study. We utilized the Morlet wavelet analysis tool (Torrence & Compo 1998) with the following equation:

$$\psi_n(\eta) = \pi^{-1/4} e^{i\omega_0 n} e^{-\eta^2}/2, \qquad (1)$$

to study the periodic and quasi-periodic variations in the above-mentioned time series. Here, ω_0 is a nondimensional frequency, and we have adopted $\omega_0 = 12$ for the midterm frequency (low periodic zone) range and $\omega_0 = 6$ for the low-frequency range (long periods). The wavelet analysis is a valuable tool for examining the presence of localized oscillations, both in time and frequency domains. In the case of monthly N–S asymmetry data, we have considered the definition of "absolute asymmetry $(A_a = N_{ca} — S_{ca})$" following the suggestion of

Ballester et al. (2005). For all data sets, we have considered ω_0 (nondimensional frequency) as 12 for the midterm frequency (low periodic zone) range and 6 for the low-frequency range (long periods; Torrence & Compo 1998; Ravindra et al. 2021). The cone of influence (COI), where the wavelet power reduces by a factor e^{-2} due to edge effect, is plotted with a bold dashed line. The thin black contours in the wavelet plots display the periods above 95% confidence level, assuming red-noise background (Grinsted et al. 2004). The global wavelet power spectra (GWPS), which indicates time-averaged power, has been computed in all cases. The 95% confidence level of the GWPS plots is determined following Torrence & Compo (1998). The results of the periodic variations are displayed in Figures 7, 8, 9, and 10.

We noticed that the Rieger group of periodicities appeared in all the data sets. However, they have different temporal evolution in the opposite hemispheres. In the northern hemisphere, these periods are prominent during cycles 16, 17, 18, 19, and 21. On the other hand, during cycles 17, 18, 20, and 21, they are significant in the southern hemisphere. Except for cycle 14, these types of periods are present in most of the cycles in the time series of the whole sphere and absolute asymmetry. We notice that QBOs in the range of 1.2–1.4 yr are significant in the cycles 15–21 for the northern hemisphere and whole-disk data. They were present in different phases of cycles 18, 19, 20, and 21 in the southern hemisphere, whereas they appeared during cycles 16, 18, 19, 20, and 21 in the asymmetry index. These indicate that the existence of Rieger-type periods as well as QBOs (1.2–1.4 yr) are different in the opposite hemispheres. A big contour of varying periods from 2–4 yr was significant for cycles 15–21 in the northern hemisphere, total sphere, and asymmetry data. In the southern hemisphere, these types of QBOs stand out reliably only after the maximum phase of cycle 18 to the onset of cycle 21. A long contour of length 5 yr appeared from 1935 to 1970, covering cycles 17–20 in the asymmetry data set, but is not much prominent in other time series. The wavelet power spectrum exhibits solar cycle periodicity in the range of 9–11 yr in all data series under study. The global wavelet power spectra of the different time series also exhibit similar kinds of statistically significant periods, and the results are consistent with the local wavelet spectra.
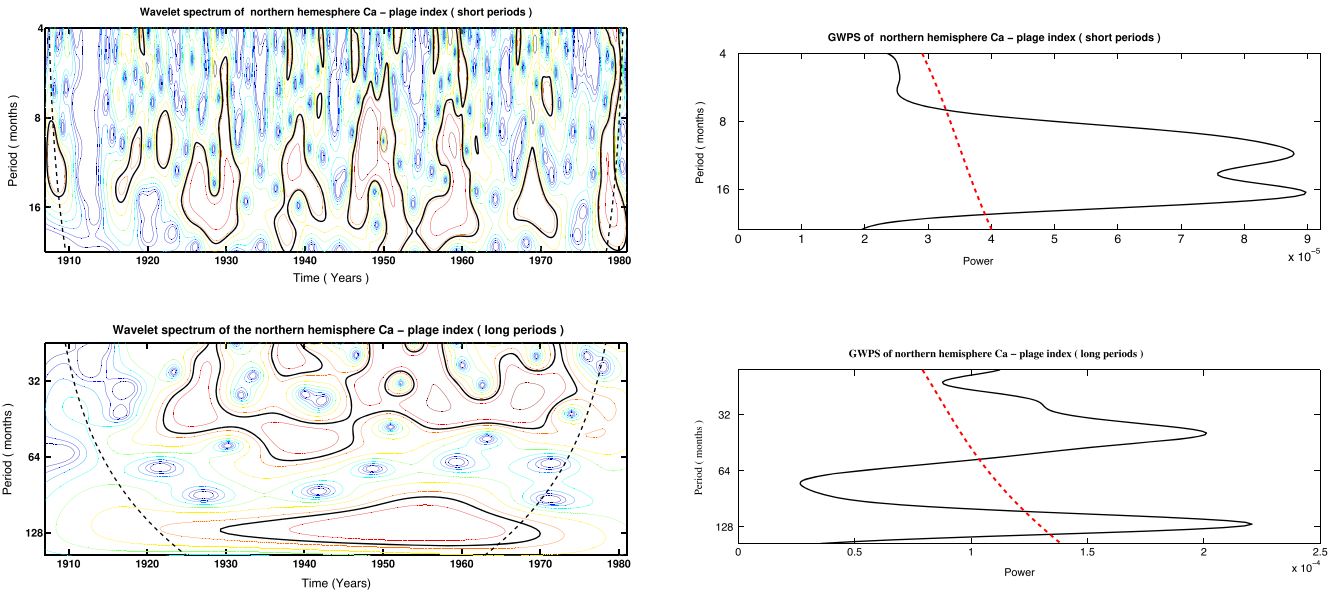
Figure 7. Top left: Morlet wavelet spectra of the monthly Ca–K index in the northern hemisphere for 1907–1980. Bottom left: local wavelet power spectra for the range 16–130 months to study the nature and variations of QBOs. Top right: global power spectra for the range 4–16 months to study Rieger-type periodicities. Bottom right: similar to top-right panel for other long term periods. Dotted lines in all global power spectra indicate a 95% confidence level.
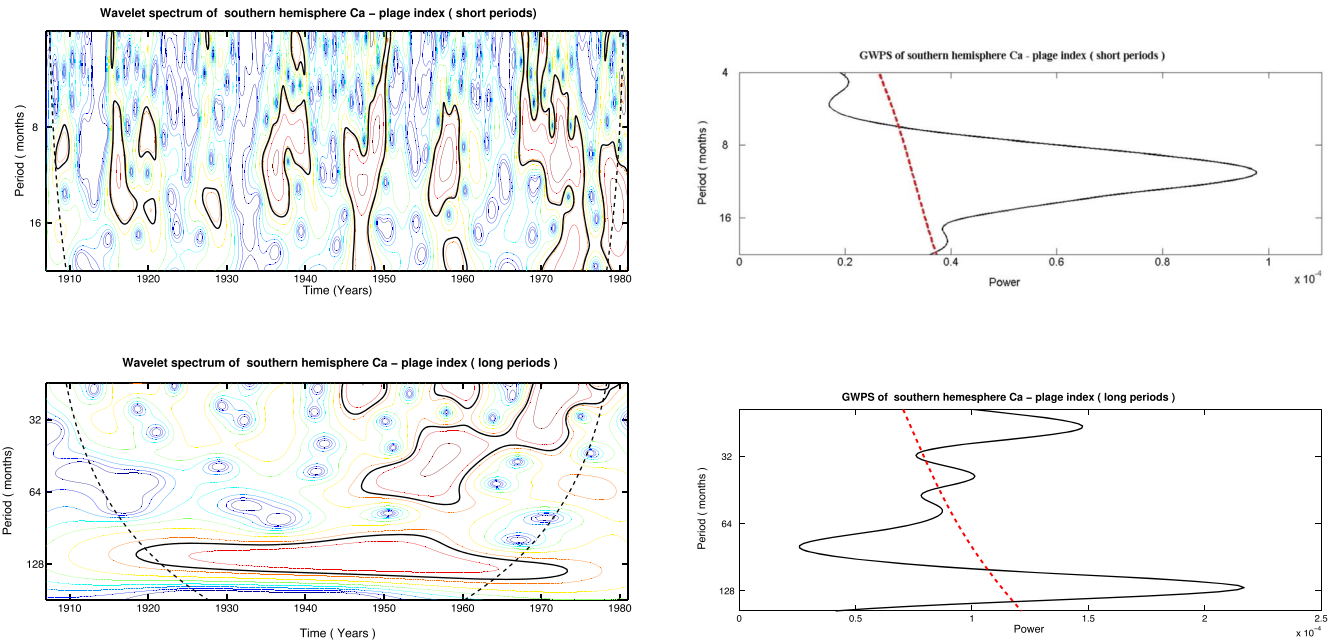
Figure 8. Top left: Morlet wavelet spectra of the monthly Ca–K index in the southern hemisphere for 1907–1980. Top right: global power spectra for the range 4–16 months to study Rieger-type periodicities. Bottom left: local wavelet power spectra for the range 16–130 months to study the nature and variations of QBOs. Bottom right: similar to top-right plot for other long term periods. Dotted lines in all global power spectra indicate a 95% confidence level.

### 3.5. Time Delay and Phase Distribution between the Hemispheres

Several studies indicated that solar indices have a phase shift or time lag/lead between the opposite hemispheres in a sunspot cycle (Temmer et al. 2006; Li 2009, etc.). To probe this time delay between the opposite hemispheres, we have calculated the cross-correlation between the monthly mean Ca–K index data of both the hemispheres following Chowdhury et al. (2019). We have calculated the cross-correlation coefficients for the different cycles using various time-lags (0, ± 1, ± 2, ..., ± 60 months), and the results are displayed in Figure 11. Here,

positive (negative) cross-correlation coefficients indicate that the Ca–K index in the northern hemisphere leads (lags) those in the southern one. The results are also listed in Table 2.

We notice from Table 2 that in cycles 17, 18, and 19, the southern hemisphere leads by about 4, 9, and 6 months, respectively. On the other hand, the northern hemisphere leads by around 2 and 8 months in cycles 16 and 20. In the rest of the cycles, no delay is observed between the hemispheres.

The cross-correlation technique to investigate time lead/lag considers the entire length of any solar cycle, but the phase shift between the hemispheres may occur during the cycle progress (Zolotova & Ponyavin 2007; Norton &
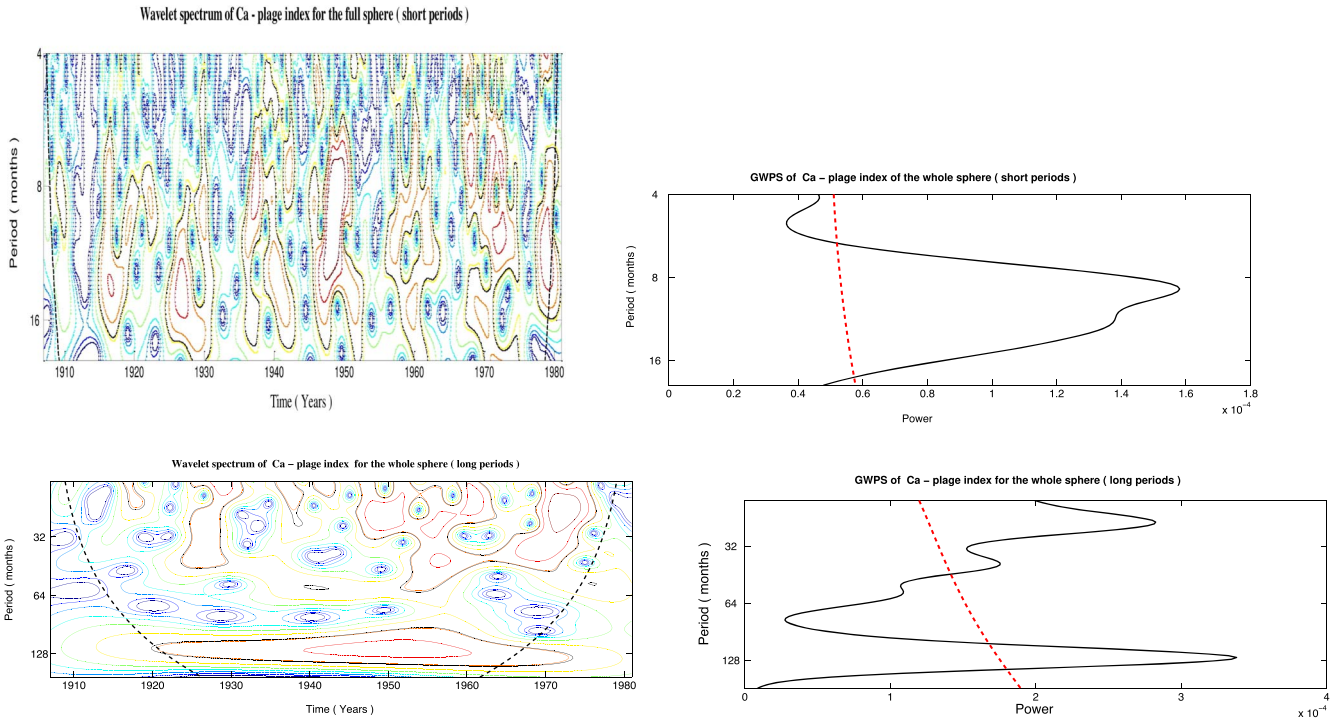
Figure 9. Top left: Morlet wavelet spectra of the monthly Ca–K index in the whole solar disk for 1907–1980. Top right: global power spectra for the range 4–16 months to study Rieger-type periodicities. Bottom left: local wavelet power spectra for the range 16–130 months to study the nature and variations of QBOs. Bottom right: similar to the top-right plot for other long term periods. Dotted lines in all global power spectra indicate a 95% confidence level.
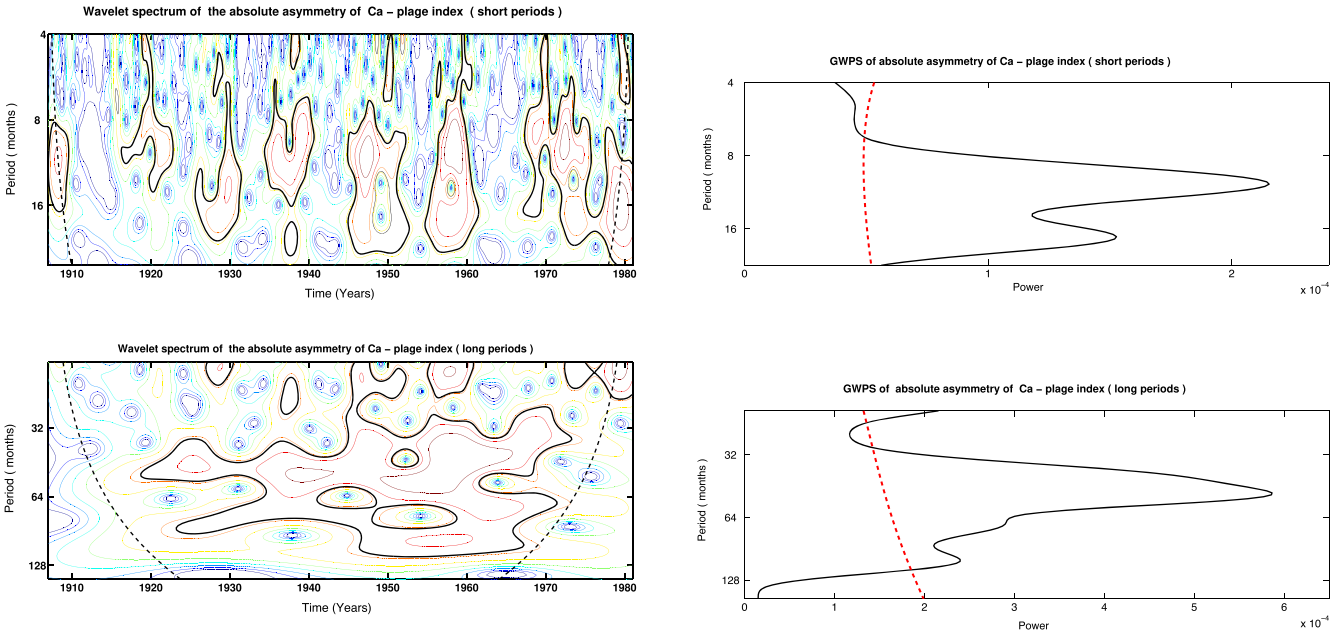

Figure 10. Top left: Morlet wavelet spectra of the monthly absolute asymmetry of the Ca–K index for 1907–1980. Bottom left: global power spectra for the range 4–16 months to study Rieger-type periodicities. Top right: local wavelet power spectra for the range 16–130 months to study the nature and variations of QBOs. Bottom right: similar to top-right plot for other long-term periods. Dotted lines in all global power spectra indicate a 95% confidence level.

Gallagher 2010; Ravindra et al. 2021, etc.). Due to this reason, we have applied the wavelet-coherence method for better understanding the relative-phase relationship and common quasi-periods of the Ca–K index data between the opposite hemispheres. The cross-wavelet coherence represents the correlation between the spectrums of two signals. This method consists of cross-wavelet transformation (XWT) and wavelet transforms coherence (WTC) techniques, where the XWT spectrum reveals localized similarity (covariance) in time and scale (period). On the other hand, the WTC spectrum measures the phase relationship between two data sets. even if the common power is low in the XWT spectrum (Maraun & Kurths 2004; Grinsted et al. 2004). In both cases, the phase relation between the two data sets is represented by arrows. The following convention is used to indicate the directions of arrows: arrows pointing right are in-phase; pointing left are in
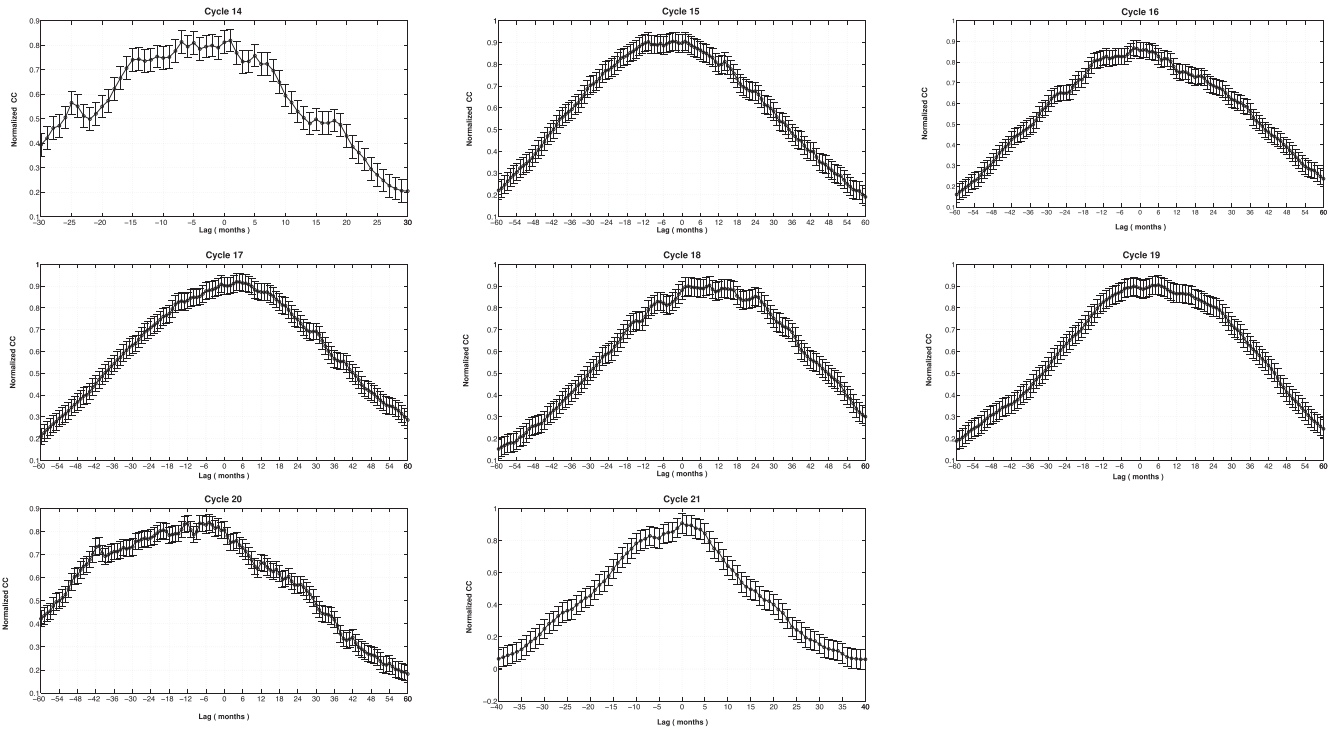
Figure 11. Cross-correlation analysis of the hemispheric Ca–K index in Solar Cycles 14–21. The abscissa indicates the lead and lag time-shifts of the southern hemisphere with respect to the northern one, with positive (negative) values representing lead (lag) time-shifts.
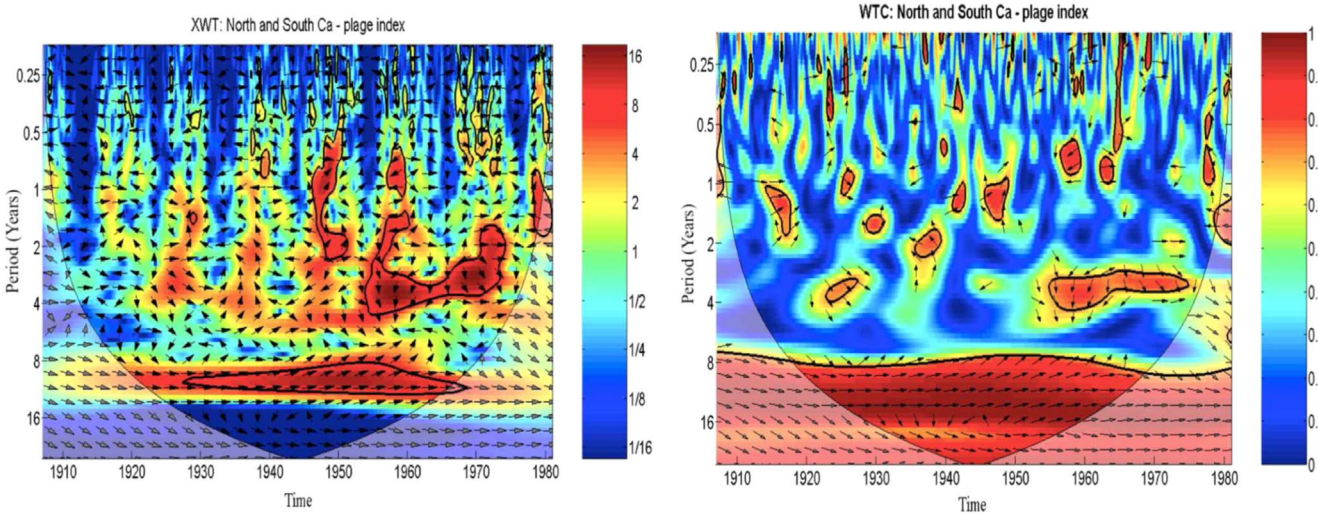

Figure 12. Left: cross-wavelet power (XWT), and right: wavelet coherence (WTC) spectra between northern and southern hemisphere Ca–K index data series for cycles 14–21. The thick black contours indicate a 95% confidence level in both Figures, and the thin line indicates the cone of influence (COI). Arrows indicate the phase relationship.

Table 2
Time Delay (in months) of Hemispheric Ca–K Index

Cycle No.	Normalized CC (95% sig. lev.)	Lag (months)
14 (d-phase only)	0.82 ± 0.04	0
15	0.91 ± 0.04	0
16	0.86 ± 0.03	−2
17	0.91 ± 0.03	4
18	0.90 ± 0.04	9
19	0.90 ± 0.04	6
20	0.83 ± 0.03	−8
21 (r-phase only)	0.90 ± 0.06	0

antiphase; arrows pointing up mean the second series leads by 90°; arrows pointing down mean the first series leads by 90°. Several researchers used XWT and WTC tools to explore the asynchronous behavior between the opposite hemispheric activities (e.g., Li et al. 2010; Deng et al. 2016; Chowdhury et al. 2019, and the references therein). Figure 12 represents the XWT and WTC plots under the red noise background, with a 95% confidence level following the recipe by Grinsted et al. (2004). After normalization of the individual spectrum in WTC, wavelet coherency takes a value between 0 and 1. The value 1 in the WTC plot indicates a perfect linear correlation between the two time series at the particular time and frequency.
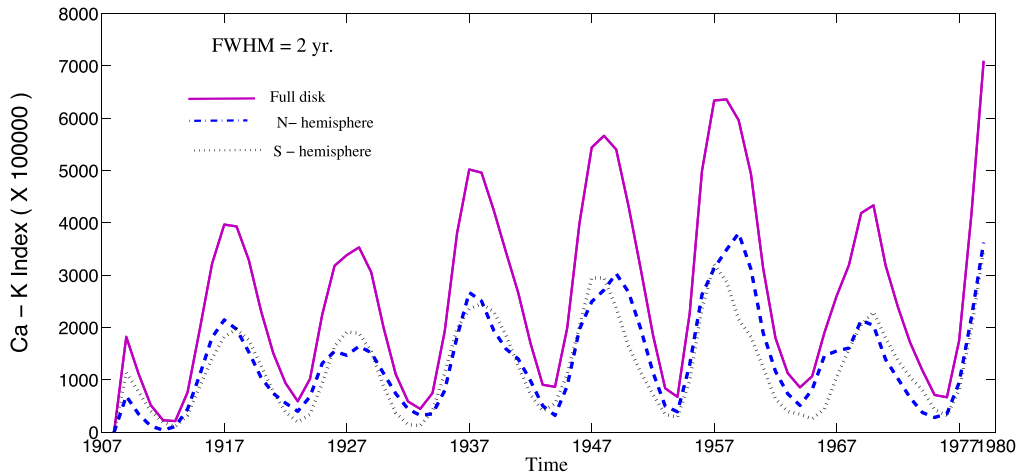
Figure 13. Plot of the smoothed Ca–K index (using a Gaussian function with a FWHM of 2 yr) for the northern hemisphere (dashed blue), the southern hemisphere (dotted blue), and the full solar disk (solid violet). All the data of Ca–K index is multiplied by a constant factor 100,000.

From the XWT plot, we notice that Rieger and Rieger-type periods and QBOs are prominent and common in both hemispheres. However, QBOs are mainly appeared from the onset of cycle 18 and continue until cycle 21. But, we did not find any regular oscillatory pattern in these periodic zones. From the WTC spectrum we found that in the vicinity of around 9 yr period, from 1935 to around 1965 (∼30 yr), the arrows were directed in the upward direction which indicates that the southern hemisphere was leading. These findings are consistent with the previous findings of Zolotova et al. (2010) who reported that sunspot area in the southern hemisphere was preceded from 1928 to 1968. However, the WTC spectrum indicates a high degree of correlation in this periodic belt. In the sunspot cycle periodic range (10–11 yr), arrows are mainly toward the right direction, which indicates a length of asymmetry between the two hemispheres. From the WTC spectrum, it is evident that this periodic belt is common to both the hemispheres and is strongly correlated.

### 3.6. Validation of the Waldmeier Effect

Waldmeier (1935) reported that the peak amplitude and rise time of different solar activity indices were anticorrelated, i.e., stronger sunspot cycles require less time to ascend and vice versa (Waldmeier effect 1). On the other hand, the rising rate and the peak amplitude of a solar cycle were strongly correlated (Waldmeier effect 2). Previous works concentrated on studying these effects considering the data of the full solar disk only. We were interested in checking whether these phenomena occur in the opposite hemispheres separately or not. So, to investigate these two effects, we utilized Ca–K index data of both the hemispheres separately and the full-disk data. We first smoothed all the data sets using a Gaussian filter with an FWHM of 2 yr as suggested by Mandal et al. (2017) and plotted them in Figure 13. We considered the rise time as the time interval between 20% and 80% of the peak value (Karak & Choudhuri 2011). Here, the rising rate is defined as the slope of the ascending part of a solar cycle.

Figure 14 represent the Waldmeier effects in the northern hemisphere, southern hemisphere, and full disk, respectively. We noticed that Figure 14(top, middle and bottom left) indicates an anticorrelated behavior between the cycle peak amplitude and the cycle rise time. On the other hand, a positive correlation is found between cycle peak amplitude and cycle

rise rate in Figure 14(top, middle and bottom right). It was also detected the basic trends of these two effects. These results validate the Waldmeier effect in the Ca–K index time series. The Waldmeier effect is not quite evident in the Ca–K data. As shown in the left panels of Figure 14, the fit is mostly driven by the outliers corresponding to cycle 20 and cycle 21. The tendency for the Waldmeier effect is better observed for cycles with low-to-moderate amplitude. For cycles with moderate-to-high amplitudes, the tendency flattens and may be hard to detect (see Figure 28 in Hathaway 2015). Also the rise time is too short as compared with Hathaway (2015). In Figure 28 in Hathaway (2015), the raise times are between 38 and 80 months (3.1–6.6 yr); this could be due to the methodics for identifying "raise phase."

3.7. Identification of the Gnevyshev Gap

There exists a gap between the ascending and descending phases of the solar cycles, and this gap is known as the Gnevyshev gap (GG; Gnevyshev 1977). The gap between the double peaks is named as GG by Storini et al. (2003). The GG is an indicator of the solar magnetic field reversal and is associated with the double-peaked structure of the solar cycles (Schatten 2009; Du 2015). To identify the existence of the GG in the Ca–K index time series under study, we have followed the method of Norton & Gallagher (2010) for cycles 15–20. A running mean of four months was applied on the data points to make it smooth. The primary and secondary maxima were identified. The period of time between the primary and secondary maxima over which the Ca–K index is lower than primary maximum is considered as the GG. Figure 15 represents such a plot for the solar cycle 18, and we readily notice the presence of the GG in the full disk and both of the hemispheres. Table 3 represents the presence/absence of the GG in solar cycles 15–20. Both northern and southern hemispheres have shown the existence of the GG in all cycles 15–20. However, it was absent in full-disk data during cycles 17 and 19. The GG and double-peaked structure of different solar cycles indicate that this is an inherent property of the hemispheres, and some physical mechanism is responsible for this phenomenon.
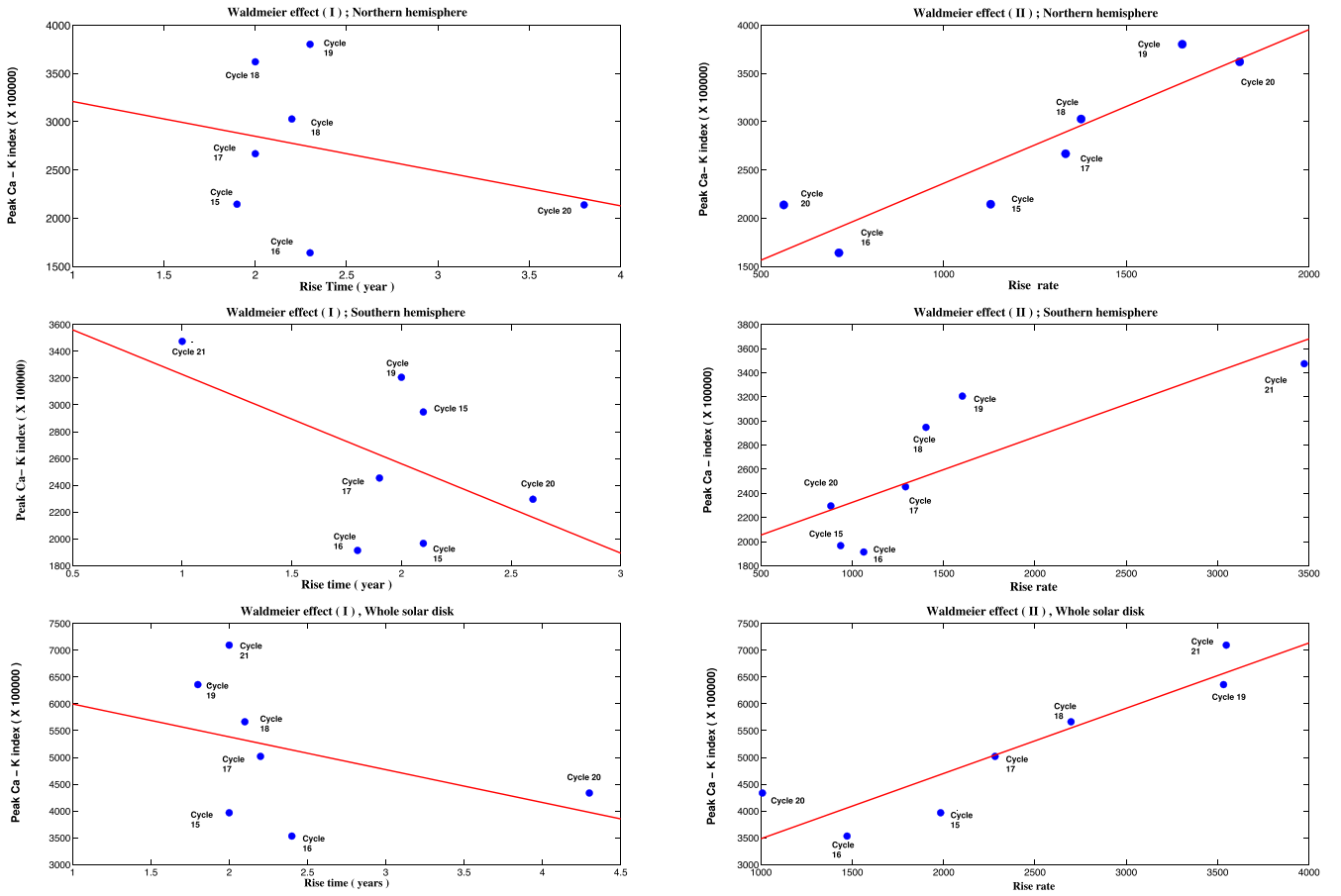
Figure 14. Top left: scatter plot of the rise time (in years) and the peak amplitude for the same solar cycles for northern hemisphere. The solid line represents the best linear fit. Solar cycle numbers are also marked by the blue circles. Top right: scatter plot of the rise rate (plage index/year) and the peak amplitude for the same solar cycles for northern hemisphere. Solar cycle numbers are also marked by the blue circles. Middle: same as top-left and right-side plots, but for the southern hemisphere. Bottom: same as top-left and right-side plots, but for the full solar disk.

4. Discussion and Conclusions

It is generally assumed that a complex magnetohydrodynamic dynamo process operating at the base of the solar convection zone generates the magnetic field. This is the primary source for the formation of sunspots, plages, and other active features on the solar surface (Hathaway 2015). Chromospheric features like Ca–K index or Ca–K plages of the Sun can be used as a proxy to study the solar magnetic fields, even when sunspots are absent in the disk. The magnetic field in Ca–K plages varies between few 10 to about a 1000–2000 Gauss in magnetic flux density (Leighton 1959; Harvey & White 1999; Ortiz & Rast 2005; Pevtsov et al. 2016), and plages usually follow ∼11 yr dominant periodic behavior. Here we have utilized the Ca–K index time series derived from the digitized Ca–K images measured at Kodaikanal Observatory during 1907–1980 to study the long-term evolution of this chromospheric emission. Our investigation also covers the nature of hemispheric asymmetry, periodic and quasi-periodic oscillations, and several distinctive properties of this parameter and their solar cycle variations. From this study, we found the following:

1. We have noticed that both the strength and temporal variation of the Ca–K index are not the same in the northern and southern hemispheres. The nature of ascendant and peak time is also different in both hemispheres in many solar cycles. We observed a maximum strength of plage index during solar cycle 19 and a minimum during cycle 16 in both hemispheres. Most of the cycles under study showed double-peaked nature around the maximum phase. This result is consistent with the temporal evolution of recently digitized sunspot area time series measured at the Kodaikanal Observatory (Ravindra et al. 2021). Further, we compared our data with the digitized long-term MWO plage data and observed a good consistency between the two time series with strong correlation. Some differences between MWO and KO plage data could be related to a slight difference in bandpass of instruments (i.e., 0.5 Å for KO and 0.35 Å for MWO).

2. We have studied the solar cycle variation of the Ca–K index of both the hemispheres within the latitude belt ±40°, which is the seat of a strong magnetic field, and found a close association with the sunspot area data sets. We find that the long-term Ca–K index in both the hemispheres and full disk follows an exponential distribution. Except for cycle 18 in the southern hemisphere, the Ca–K index follows the odd–even cycle rule. Sunspot area data measured at Royal Greenwich Observatory (RGO) as well as at the Kodaikanal Observatory also indicates that amplitude of cycle 18 is higher than cycle 17 and thus breaks the odd–even rule for cycle 18 (Li et al. 2019; Ravindra et al. 2021).
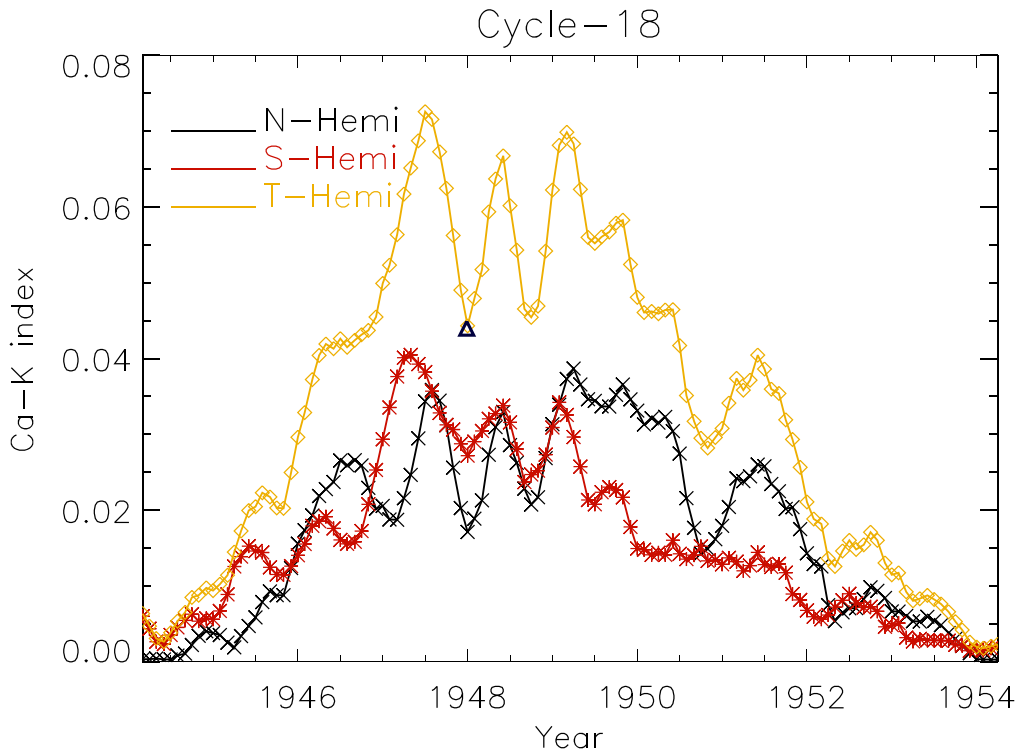
Figure 15. Determination of the Gnevyshev gaps in Ca–K index and is shown here for the northern hemisphere (black ×), southern hemisphere (red ⋆), and the whole Sun (yellow ◊) for solar cycle 18.

Table 3
Gnevyshev Gap for the Northern and Southern Hemispheres and Whole-disk Data

Cycle No.	N hemi	S hemi	Total
15	P	P	P
16	P	P	P
17	P	P	A
18	P	P	P
19	P	P	A
20	P	P	P

Note. In the Table, N hemi stands for the northern hemisphere, and S hemi stands for the southern hemisphere. P and A represent the presence and absence, respectively, of double peaks in the cycle.

3. The magnitude of the N–S asymmetry is not very high and has maximum value around the minima or the onset of any new cycle, and it shows some kind of cyclic trend. The northern hemisphere was dominant during cycles 14 (descending phase) and 19. In other solar cycles, asymmetry was not statistically significant. Our cumulative analysis revealed that the northern hemisphere was more active in cycles 15, 18, 19, and 20, whereas for cycles 14 (decay phase) and 17, activities were more prominent in the southern one. This result of cumulative count is closely consistent with the results of Zhang & Feng (2015) who utilized long-term sunspot area data measured at Greenwich Observatory and showed that the northern hemisphere was more active in cycles 15, 16, 18, 19, and 20, whereas the southern hemisphere was more prominent in cycle 17. However, sunspot area observations at Kodaikanal Observatory indicated that the northern hemisphere was more prominent in all cycles from 16 to 19 (Ravindra et al. 2021).

4. The northern hemisphere led in cycles 16 and 20 by 2 and 8 months, respectively. On the other hand, the southern hemisphere was leading in cycles 17, 18, and 19 and the time delay ranged from 4 to 9 months. In the rest of the cycles, the time lag was not observed.

5. Our power spectral analysis method detected several midterm periodicities, including the Rieger group and QBOs, separately in the northern and southern hemispheres, total disk, and the asymmetry data set. However, the temporal evolution of these periods is different in the opposite hemispheres. We have observed that Rieger-type periods and QBOs have the N–S asymmetry in existence in the Ca–K index time series. This result is consistent with the findings of Gurgenashvili et al. (2017). Long-term periods like 4–5 yr were very prominent in asymmetry data. We notice that the Ca–K index time series has prominent 11 yr cycle variations. The cross-wavelet analysis indicated that both Rieger-type periods and QBOs are common and statistically significant in both the hemispheres with phase asynchrony. We noticed that phase coherency exists only in a narrow period belt of 9–12 yr, including the sunspot cycle. Therefore high-frequency (low-period) components demonstrate noisy behavior with phase mixing and phase synchronization is detected mainly in the low-frequency modes (long periods).

6. Using the Ca–K index time series, we confirmed the Waldmeier effect in both the hemispheres separately and in the entire solar disk. Finally, we have detected the Gnevyshev Gap for individual solar cycles 15–20. We have found that this phenomenon is common in Ca–K index data of the northern and southern hemispheres for all cycles. However, it is absent during cycles 17 and 19 in the whole solar disk. The results of GG in Ca–K index

are closely consistent with the GG detected in the Kodaikanal sunspot area data set (Ravindra et al. 2021).

Our analysis has detected the Rieger-type and QBOs in the Ca–K index time series, which has also been reported by different authors using different solar activity indices, including helioseismic proxies (Cadavid et al. 2005; Knaack et al. 2005; Chowdhury et al. 2009, 2013, 2016, 2019; Fletcher et al. 2010; Katsavrias et al. 2012; Kilcik et al. 2018, 2020; Gurgenashvili et al. 2017; Deng et al. 2016; Ravindra et al. 2021, and the references therein). There is currently no physical model explaining all aspects of the origin of different types of midterm periods. These midterm periods might be related to the periodic emergence of magnetic flux from the deep solar interior (Ballester et al. 2002) or the dynamics of Rossby-type waves in the solar atmosphere (Lou 2000; Ulrich 2001; Gurgenashvili et al. 2016, etc.).

McIntosh et al. (2015) indicated that the observed periodicities in the range of 5–8 months (Rieger-type periods) are generated due to the interaction between two oppositely signed magnetic activity bands seated in the deep interior of the opposite hemispheres. Further, Zaqarashvili (2018) studied the instability inside the tachocline and indicated a close relationship between slow magneto-Rossby waves and long-term variations of solar activity. The interactions between torsional oscillation and large-scale convection generate these types of waves on the solar surface and determine the rate of their variation. There is a close link between the Rossby-type waves and the solar dynamo as the torsional oscillations have closely connected to the latitude of magnetic activity.

Recently, Gachechiladze et al. (2019) argued that fast global magneto-Rossby waves with wavenumber $m = 1$ and $n = 3, 4, 5,$ and 6 could produce periodicities like Rieger type, 240–270 days, 310–320 days, and 380 days, respectively, and that other observed higher-order periods are generated due to magneto-Kelvin waves. The growth rates of these Rossby-type waves in the solar interior are very sensitive to the magnetic field strengths. Also, see Dikpati et al. (2020) and Zaqarashvili et al. (2021) for detailed investigations about the shallow-water MHD model, the interaction between magnetic Rossby waves, and tachocline instabilities and their relationship with different solar periodicities. The existence of such Rossby-type waves in the solar interior has been confirmed by Liang et al. (2019) using time-distance helioseismology of N–S subsurface zonal flows, by Hanson et al. (2020) using ring-diagram flow maps in the GONG ++ project, and in the solar atmosphere by McIntosh et al. (2017) utilizing coronal data from Solar Terrestrial Relations Observatory (STEREO) and Solar Dynamics Observatory (SDO). On the other hand, some researchers (Benevolenskaya 1998; Obridko & Badalyan 2014; Strugarek et al. 2018, etc.) proposed that QBOs are connected with the mechanism of the second dynamo situated near the solar surface. Ulrich & Tran (2013) made a detailed analysis of the structure and spatio-temporal evolution of the solar magnetic field and hinted that the QBOs are linked to the solar dynamo mechanism. Inceoglu et al. (2019) used dynamo simulations in the long-term sunspot area data. They argued that the turbulent α-effect at the bottom of the solar convection zone is more effective in producing QBOs. More investigation on solar interior dynamics is required to explore the reasons behind the different types of periodicities present in solar activity indices.

Our cross-correlation analysis and cross-wavelet technique indicated a time lag/lead or phase asynchrony between the hemispheric Ca–K activities in most of the solar cycles. Such type of phase asynchrony between the northern and southern hemispheric activities was reported time-to-time by several authors (Donner & Thiel 2007; Zolotova et al. 2009; Muraközy 2016; McIntosh et al. 2013; Ravindra et al. 2021, etc.). Previous studies show a correlation between the hemispheric asymmetry and this time lag/lead, and the whole phenomena are also correlated with the variation of the global solar cycle period (McIntosh & Leamon 2014; Zhang & Feng 2015; Schüssler & Cameron 2018, and the references therein). Shukuya & Kusano (2017) argued that the time lag/lead and phase shift between the opposite hemispheres is an inherent characteristic of mean-field dynamo solutions related to the magnetic Reynolds number for the solar convection zone. Through cross-wavelet analysis, we find that phase coherency between the opposite hemispheres is only present in a narrow frequency range inside the periodic belt of 8–14 yr follows the conclusions of Donner & Thiel (2007); Deng et al. (2016).

We have made a detailed analysis of the hemispheric imbalance of the Ca–K index and their statistical significance. This N–S asymmetry may play a significant role in determining the behavior of the solar cycle. Our result of the statistical significance of the asymmetry index indicating that the solar cycle evolution of the plage magnetic field originating in both the hemispheres are weakly coupled. Figure 5(left panel) exhibits a transition of the asymmetry index from positive to negative values. Probably, this is a part of the variation in asymmetry with a period of 100–110 yr (Badalyan & Obridko 2011). The exact reason behind this asymmetry and its variations are still unknown. However, it has been argued that the random nature and fluctuations in the Babcock-Leighton type dynamo process of poloidal field generation may play a key role in producing this effect (Goel & Choudhuri 2009; Norton et al. 2014; Passos et al. 2014); asymmetric nature of the meridional flow (Hathaway & Rightmire 2010; Upton & Hathaway 2014; Belucz & Dikpati 2013); nonlinear coupling between the dipolar and quadrupolar components of the solar magnetic fields and long term-parity violation (Hazra & Nandy 2019); asymmetry in the helioseismic zonal flows in different latitude bands (Komm et al. 2014, 2020, etc.), and even the presence of relict magnetic field in the Sun (Cowling 1945; Sonett 1983). In addition to N–S asymmetry in developing magnetic features, the magnetic activity originating in one hemisphere may cross solar equator and contribute to activity in other hemisphere. The cross-equatorial flux transport was noted by Cameron et al. (2013), Mordvinov et al. (2016). Virtanen et al. (2018) found that because of trans-equatorial flux transport, even if activity is limited to a single hemisphere, regular pattern of polar magnetic fields will develop in both hemispheres albeit with some delay as compared with when the activity is present in both hemispheres.

The observed long-term preferred asymmetry of the plages in the northern hemisphere, during the cycles 15 to 16 and 18 to 20, probably related to the tendency of the clustering of the low-latitude magnetic field at "preferred longitudes" that contain some complex active regions which may last for several solar rotations up to several solar cycles (Temmer et al. 2006). The value of the asymmetry index probably indicates

the difference between dynamo magnetic field strengths in the opposite hemispheres, but the mechanism of the difference is still not clear. Probably, this hemispheric asymmetry may exhibit a quantitative measure about the properties of some unknown mechanism that governs the actual degree of similarity in the evolution of active processes in the opposite hemispheres in the course of the solar cycle. We have found that only in cycle 19 and the descending phase of cycle 14, the asymmetry is statistically significant. The value of the asymmetry in different solar cycles is not very high. Recently, Bertello et al. (2020) have reported the absence of hemispheric asymmetry in the Ca–K index time series measured at the Mount Wilson Observatory starting from 1915 to 1985. This weak nature of asymmetry in chromospheric emission may suggest a difference in the dynamical behavior between stronger/large-scale (sunspots) and weaker/small-scale (plages) magnetic field regions during different episodes of the sunspot cycle. Probably the turbulent dynamo may have a complex nature to produce large-scale and small-scale fields.

The present analysis confirmed the Waldmeier effect, and we have validated this effect in both the hemispheres separately along with the whole solar disk. This effect was previously reported in sunspot number/area data sets (Takalo & Mursula 2018; Chowdhury et al. 2019) and recently in the stellar cycle data (Garg et al. 2019). This Waldmeier effect is one of the distinctive features of solar activities and can predict the strength of the ongoing/upcoming cycle (Nagovitsyn & Kuleshova 2012; Chowdhury et al. 2021). This phenomenon correlates the time of increase in solar activity from minimum to maximum with the magnitude of the maximum. Further, using sunspot number data, Nagovitsyn & Kuleshova (2012) showed that it can be modified by considering the ratio between the maximum average annual growth rates of activity on the ascending branch of the solar cycle with the maximum height. Utilizing this method, the above mentioned authors predicted maximum sunspot number of the cycle 24 as 104 (±12), and time of maxima in 2013 or later which was very close to the observed one. We are interested to utilize this technique in Ca II K data set in future. Yeates et al. (2008) argued that during weak meridional circulation, the cycle period and the ascending time becomes longer. During this extended cycle period, the turbulent diffusion also works for a longer time, making the cycle amplitude weaker. Pipin & Kosovichev (2011) reported that hemispheric asymmetry and Waldmeier effect depend on the turbulent diffusivity and differential rotation near-surface layer and the magnetic helicity dissipation rate.

We have detected a solid correlation between the Ca–K index and sunspot area in both the northern and southern hemispheres and the whole-disk data within the low latitudes. Bertello et al. (2016) also reported such a strong correlation between the revised sunspot number and the Ca–K emission index. Mandal et al. (2017) observed a correlation between sunspot area and Ca–K plage area considering the integrated whole-disk time series only. This indicates that the solar atmosphere at different heights is magnetically coupled, and the dynamo responsible for generating weak (plages) and strong magnetic fields (sunspots) in the solar layers. Our data show that the relationship between sunspot and plage area (Figure 4) becomes nonlinear for very large sunspot areas. This nonlinearity may suggest that for large sunspot groups, strong magnetic fields (sunspots) represent larger fraction of total magnetic flux of active regions as compared with smaller active

regions. This interesting conjecture deserves additional investigation.

We have noticed several complex behaviors in the Ca–K index cycles like double-peak, peak-type spikes, and Gnevyshev gap. These are real features reported in sunspot-related data sets (Norton & Gallagher 2010; Ravindra et al. 2021, etc.,) and geomagnetic indices (Takalo 2021). Similar types of complex patterns are also observed in the MWO Ca–K plage data sets. So far, there is no physical model or analytical formula that can reasonably explain these features. Du (2015) suggested that any solar cycle is governed by a bidynamo model, where the first one is the standard dynamo. The second one works either in the rising or descending episodes as a long stochastic perturbation producing the double peak in the sunspot cycle. Several authors tested this type of bimodal distribution and successfully explained some of the complex natures of the solar cycle (Muñoz-Jaramillo et al. 2015; McClintock & Norton 2016; Nagovitsyn & Pevtsov 2016; Tlatov et al. 2019, and references therein). Dikpati et al. (2018) proposed that energy exchange among magnetic fields, Rossby-type waves, and differential rotation in the solar tachocline can generate nonlinear quasi-periodicities, which in turn relate to the observed spikes in solar activity cycles. On the other hand, Karak et al. (2018) argued that fluctuations in the Babcock–Leighton type of dynamos could produce short-term fluctuations in the polar field formation. These fluctuations can influence the toroidal field formation, which is the cause of double peaks and GG in the next solar cycle.

The spatio-temporal evolution of the Ca–K plage index and their different properties play a significant role in understanding the formation of the solar magnetic field and its relation to various activity manifestations. For the last two decades, different complex characteristic properties of the solar cycles, solar magnetism as well as cycle forecasting have been modeled in great detail using the Babcock–Leighton-type of dynamo models (Choudhuri et al. 2007; Cameron et al. 2017; Charbonneau 2020; Hazra & Nandy 2019; Obridko et al. 2021, etc.). However, the existing dynamo models are insufficient to fully explain the irregularities in cycle length and amplitude, the N–S asymmetry, and the double-peaked structure in a solar cycle. More knowledge about solar magnetic flux generation and their cyclic variations are required to understand the intrinsic mechanism responsible for these phenomena. In future, we aim to perform more work on these topics of Ca–K plage data from other observatories and compare with our findings.

ORCID iDs

Partha Chowdhury ● https://orcid.org/0000-0003-3253-9054
Ravindra Belur ● https://orcid.org/0000-0003-2165-3388
Luca Bertello ● https://orcid.org/0000-0002-1155-7141
Alexei A. Pevtsov ● https://orcid.org/0000-0003-0489-0920

References

Badalyan, O. G., & Obridko, V. N. 2011, NewA, 16, 357
Ballester, J. L., Oliver, R., & Carbonell, M. 2002, ApJ, 566, 505
Ballester, J. L., Oliver, R., & Carbonell, M. 2005, A&A, 431, L5
Bazilevskaya, G., Broomhall, A. M., Elsworth, Y., & Nakariakov, V. M. 2014, SSRv, 186, 359
Belucz, B., & Dikpati, M. 2013, ApJ, 779, 4
Benevolenskaya, E. E. 1998, ApJL, 509, L49
Bertello, L., Pevtsov, A., Tlatov, A., & Singh, J. 2016, SoPh, 291, 2967
Bertello, L., Pevtsov, A. A., & Ulrich, R. K. 2020, ApJ, 897, 181
Bertello, L., Ulrich, R. K., & Boyden, J. E. 2010, SoPh, 264, 31
Cadavid, A. C., Lawrence, J. K., McDonald, D. P., & Ruzmaikin, A. 2005, SoPh, 226, 359
Cameron, R. H., Dasi-Espuig, M., Jiang, J., et al. 2013, A&A, 557, A141
Cameron, R. H., Dikpati, M., & Brandenburg, A. 2017, SSRv, 210, 367
Carbonell, M., Oliver, R., & Ballester, J. L. 1993, A&A, 274, 497
Carbonell, M., Terradas, J., Oliver, R., & Ballester, J. L. 2007, A&A, 476, 951
Charbonneau, P. 2020, LRSP, 17, 4
Chatterjee, S., Banerjee, D., & Ravindra, B. 2016, ApJ, 827, 87
Chatzistergos, T., Ermolli, I., Krivova, N. A., & Solanki, S. K. 2018, in IAU Symp. 340, Long-term Datasets for the Understanding of Solar and Stellar Magnetic Cycles, ed. D. Banerjee et al. (Cambridge: Cambridge Univ. Press), 125
Chatzistergos, T., Ermolli, I., Krivova, N. A., & Solanki, S. K. 2019, A&A, 625, A69
Choudhuri, A. R., Chatterjee, P., & Jiang, J. 2007, PhRvL, 98, 131103
Chowdhury, P., Choudhary, D. P., & Gosain, S. 2013, ApJ, 768, 188
Chowdhury, P., Gokhale, M. H., Singh, J., & Moon, Y. J. 2016, Ap&SS, 361, 54
Chowdhury, P., Jain, R., Ray, P. C., Burud, D., & Chakrabarti, A. 2021, SoPh, 296, 69
Chowdhury, P., Khan, M., & Ray, P. C. 2009, MNRAS, 392, 1159
Chowdhury, P., Kilcik, A., Yurchyshyn, V., Obridko, V. N., & Rozelot, J. P. 2019, SoPh, 294, 142
Cowling, T. G. 1945, MNRAS, 105, 166
de Paula, V., & Curto, J. J. 2020, SoPh, 295, 99
Deng, L. H., Xiang, Y. Y., Qu, Z. N., & An, J. M. 2016, AJ, 151, 70
Dikpati, M., Gilman, P. A., Chatterjee, S., McIntosh, S. W., & Zaqarashvili, T. V. 2020, ApJ, 896, 141
Dikpati, M., McIntosh, S. W., Bothun, G., et al. 2018, ApJ, 853, 144
Donahue, R. A., & Keil, S. L. 1995, SoPh, 159, 53
Donner, R., & Thiel, M. 2007, A&A, 475, L33
Du, Z. L. 2015, ApJ, 804, 3
Ermolli, I., Criscuoli, S., Uitenbroek, H., et al. 2010, A&A, 523, A55
Ermolli, I., Shibasaki, K., Tlatov, A., & van Driel-Gesztelyi, L. 2014, SSRv, 186, 105
Ermolli, I., Solanki, S. K., Tlatov, A. G., et al. 2009, ApJ, 698, 1000
Fletcher, S. T., Broomhall, A.-M., Salabert, D., et al. 2010, ApJL, 718, L19
Fontenla, J. M., Stancil, P. C., & Landi, E. 2015, ApJ, 809, 157
Foukal, P. 1996, GeoRL, 23, 2169
Foukal, P., Bertello, L., Livingston, W. C., et al. 2009, SoPh, 255, 229
Foukal, P., Fröhlich, C., Spruit, H., & Wigley, T. M. L. 2006, Natur, 443, 161
Gachechiladze, T., Zaqarashvili, T. V., Gurgenashvili, E., et al. 2019, ApJ, 874, 162
Garg, S., Karak, B. B., Egeland, R., Soon, W., & Baliunas, S. 2019, ApJ, 886, 132
Gnevyshev, M. N. 1977, SoPh, 51, 175
Gnevyshev, M. N., & Ohl, A. I. 1948, AZh, 25
Goel, A., & Choudhuri, A. R. 2009, RAA, 9, 115
Grinsted, A., Moore, J. C., & Jevrejeva, S. 2004, NPGeo, 11, 561
Gurgenashvili, E., Zaqarashvili, T. V., Kukhianidze, V., et al. 2016, ApJ, 826, 55
Gurgenashvili, E., Zaqarashvili, T. V., Kukhianidze, V., et al. 2017, ApJ, 845, 137
Hanson, C. S., Gizon, L., & Liang, Z.-C. 2020, A&A, 635, A109

Harvey, K. L., & White, O. R. 1999, ApJ, 515, 812
Hasan, S. S., Mallik, D. C. V., Bagare, S. P., & Rajaguru, S. P. 2010, ASSP, 19, 12
Hathaway, D. H. 2015, LRSP, 12, 4
Hathaway, D. H., & Rightmire, L. 2010, Sci, 327, 1350
Hazra, S., & Nandy, D. 2019, MNRAS, 489, 4329
Inceoglu, F., Simoniello, R., Arlt, R., & Rempel, M. 2019, A&A, 625, A117
Karak, B. B., & Choudhuri, A. R. 2011, MNRAS, 410, 1503
Karak, B. B., Mandal, S., & Banerjee, D. 2018, ApJ, 866, 17
Katsavrias, C., Preka-Papadema, P., & Moussas, X. 2012, SoPh, 280, 623
Kilcik, A., Chowdhury, P., Sarp, V., et al. 2020, SoPh, 295, 159
Kilcik, A., Yurchyshyn, V., Donmez, B., et al. 2018, SoPh, 293, 63
Knaack, R., Stenflo, J. O., & Berdyugina, S. V. 2005, A&A, 438, 1067
Komm, R., Howe, R., González Hernández, I., & Hill, F. 2014, SoPh, 289, 3435
Komm, R., Howe, R., & Hill, F. 2020, SoPh, 295, 47
Krivova, N. A., Solanki, S. K., Fligge, M., & Unruh, Y. C. 2003, A&A, 399, L1
Leighton, R. B. 1959, ApJ, 130, 366
Li, K. J. 2009, SoPh, 255, 169
Li, K. J., Liu, X. H., Gao, P. X., & Zhan, L. S. 2010, NewA, 15, 346
Li, K. J., Xu, J. C., Yin, Z. Q., & Feng, W. 2019, ApJ, 875, 90
Liang, Z.-C., Gizon, L., Birch, A. C., & Duvall, T. L. 2019, A&A, 626, A3
Livingston, W., Wallace, L., White, O. R., & Giampapa, M. S. 2007, ApJ, 657, 1137
Lou, Y.-Q. 2000, ApJ, 540, 1102
Mandal, S., Chatterjee, S., & Banerjee, D. 2017, ApJ, 835, 158
Maraun, D., & Kurths, J. 2004, NPGeo, 11, 505
McClintock, B. H., & Norton, A. A. 2016, ApJ, 818, 7
McIntosh, S. W., Cramer, W. J., Pichardo Marcano, M., & Leamon, R. J. 2017, Nature Astronomy, 1, 0086
McIntosh, S. W., & Leamon, R. J. 2014, ApJL, 796, L19
McIntosh, S. W., Leamon, R. J., Gurman, J. B., et al. 2013, ApJ, 765, 146
McIntosh, S. W., Leamon, R. J., Krista, L. D., et al. 2015, NatCo, 6, 6491
Mordvinov, A., Pevtsov, A., Bertello, L., & Petri, G. 2016, STP, 2, 3
Muñoz-Jaramillo, A., Senkpeil, R. R., Windmueller, J. C., et al. 2015, ApJ, 800, 48
Muraközy, J. 2016, ApJ, 826, 145
Nagovitsyn, Y. A., & Kuleshova, A. I. 2012, ARep, 56, 800
Nagovitsyn, Y. A., & Pevtsov, A. A. 2016, ApJ, 833, 94
Norton, A. A., Charbonneau, P., & Passos, D. 2014, SSRv, 186, 251
Norton, A. A., & Gallagher, J. C. 2010, SoPh, 261, 193
Obridko, V. N., & Badalyan, O. G. 2014, ARep, 58, 936
Obridko, V. N., Pipin, V. V., Sokoloff, D., & Shibalova, A. S. 2021, MNRAS, 504, 4990
Ortiz, A., & Rast, M. 2005, MmSAI, 76, 1018
Passos, D., Nandy, D., Hazra, S., & Lopes, I. 2014, A&A, 563, A18
Pevtsov, A. A., Virtanen, I., Mursula, K., Tlatov, A., & Bertello, L. 2016, A&A, 585, A40
Pipin, V. V., & Kosovichev, A. G. 2011, ApJ, 741, 1
Priyal, M., Singh, J., Belur, R., & Rathina, S. K. 2017, SoPh, 292, 85
Priyal, M., Singh, J., Ravindra, B., Priya, T. G., & Amareswari, K. 2014, SoPh, 289, 137
Priyal, M., Singh, J., Ravindra, B., & Shekar, B. C. 2019, SoPh, 294, 131
Ravindra, B., Chowdhury, P., & Javaraiah, J. 2021, SoPh, 296, 2
Schatten, K. H. 2009, SoPh, 255, 3
Schrijver, C. J., Cote, J., Zwaan, C., & Saar, S. H. 1989, ApJ, 337, 964
Schüssler, M., & Cameron, R. H. 2018, A&A, 618, A89
Sheeley, N. R., Cooper, T. J., & Anderson, J. R. L. 2011, ApJ, 730, 51
Shukuya, D., & Kusano, K. 2017, ApJ, 835, 84
Sokoloff, D., & Nesme-Ribes, E. 1994, A&A, 288, 293
Solanki, S., & Krivova, N. 2009, LanB, 4B, 153
Sonett, C. P. 1983, Natur, 306, 670
Storini, M., Bazilevskaya, G. A., Fluckinger, E. O., et al. 2003, AdSpR, 31, 895
Strugarek, A., Beaudoin, P., Charbonneau, P., & Brun, A. S. 2018, ApJ, 863, 35
Takalo, J. 2021, SoPh, 296, 19
Takalo, J., & Mursula, K. 2018, A&A, 620, A100
Temmer, M., Rybák, J., Bendík, P., et al. 2006, A&A, 447, 735
Tlatov, A., Riehokainen, A., & Tlatova, K. 2019, SoPh, 294, 45
Torrence, C., & Compo, G. P. 1998, BAMS, 79, 61
Ulrich, R. K. 2001, ApJ, 560, 466
Ulrich, R. K., & Tran, T. 2013, ApJ, 768, 189
Upton, L., & Hathaway, D. H. 2014, ApJ, 792, 142

Virtanen, I. O. I., Virtanen, I. I., Pevtsov, A. A., & Mursula, K. 2018, A&A, 616, A134

Waldmeier, M. 1935, MiZur, 14, 105

Waldmeier, M. 1957, ZAp, 43, 149

Yeates, A. R., Nandy, D., & Mackay, D. H. 2008, ApJ, 673, 544

Zaqarashvili, T. 2018, ApJ, 856, 32

Zaqarashvili, T. V., Albekioni, M., Ballester, J. L., et al. 2021, SSRv, 217, 15

Zhang, J., & Feng, W. 2015, AJ, 150, 74

Zolotova, N. V., & Ponyavin, D. I. 2007, SoPh, 243, 193

Zolotova, N. V., & Ponyavin, D. I. 2015, Ge&Ae, 55, 902

Zolotova, N. V., Ponyavin, D. I., Arlt, R., & Tuominen, I. 2010, AN, 331, 765

Zolotova, N. V., Ponyavin, D. I., Marwan, N., & Kurths, J. 2009, A&A, 503, 197